Schweizerischer Erdbebendienst
Service Sismologique Suisse
Servizio Sismico Svizzero
Swiss Seismological Service

ETH zürich

SITE CHARACTERIZATION REPORT

SFRS: Frutigen (BE) - Schulhaus Kanderbrück

Manuel Hobiger, Dario Chieppa, Donat Fäh

Last Modification: 03/11/2021

Schweizerischer Erdbebendienst (SED)
Service Sismologique Suisse
Servizio Sismico Svizzero
Servizi da Terratrembels Svizzer

ETH Zürich
Sonneggstrasse 5
8092 Zürich
Schweiz
manuel.hobiger@sed.ethz.ch

Contents

Summary

The free-field strong-motion station SFRS was built in Frutigen (BE) close to the northern entrance of the Lötschberg Base tunnel. We performed a passive seismic array measurement to characterize the soil underneath the station.
The measurements show that the fundamental frequency of the structure beneath the station is about 2.0 Hz. Dispersion curves for Love and Rayleigh waves were retrieved between 2.2 and over 20 Hz, but the mode attribution of these curves is not straightforward. The Love wave dispersion curve was finally interpreted as belonging partly to the fundamental and partly to the first higher mode.
Inversions using the dispersion curves and the ellipticity angle as targets were performed. The underground can be mainly characterized by a single or two near-surface layers in the topmost 3.5 m, followed by another layer with shear-wave velocity of about 510 to 540 m/s down to a depth of about 66 to 79 m, where the seismic bedrock is found.
The V_{S30} value is (460.3 ± 7.2) m/s. In EC8, this corresponds to soil class B. In SIA261, it corresponds to soil class C.

1 Introduction

In the framework of the second phase of the Swiss Strong Motion Network (SSMNet) renewal project, a new station was planned in the vicinity of the northern entrance of the Lötschberg Base tunnel. The Schulhaus Kanderbrück in Frutigen (BE) was selected as installation site. The new station, called SFRS, went operational on 11 October 2018. The location of the station is shown in Fig. 1.

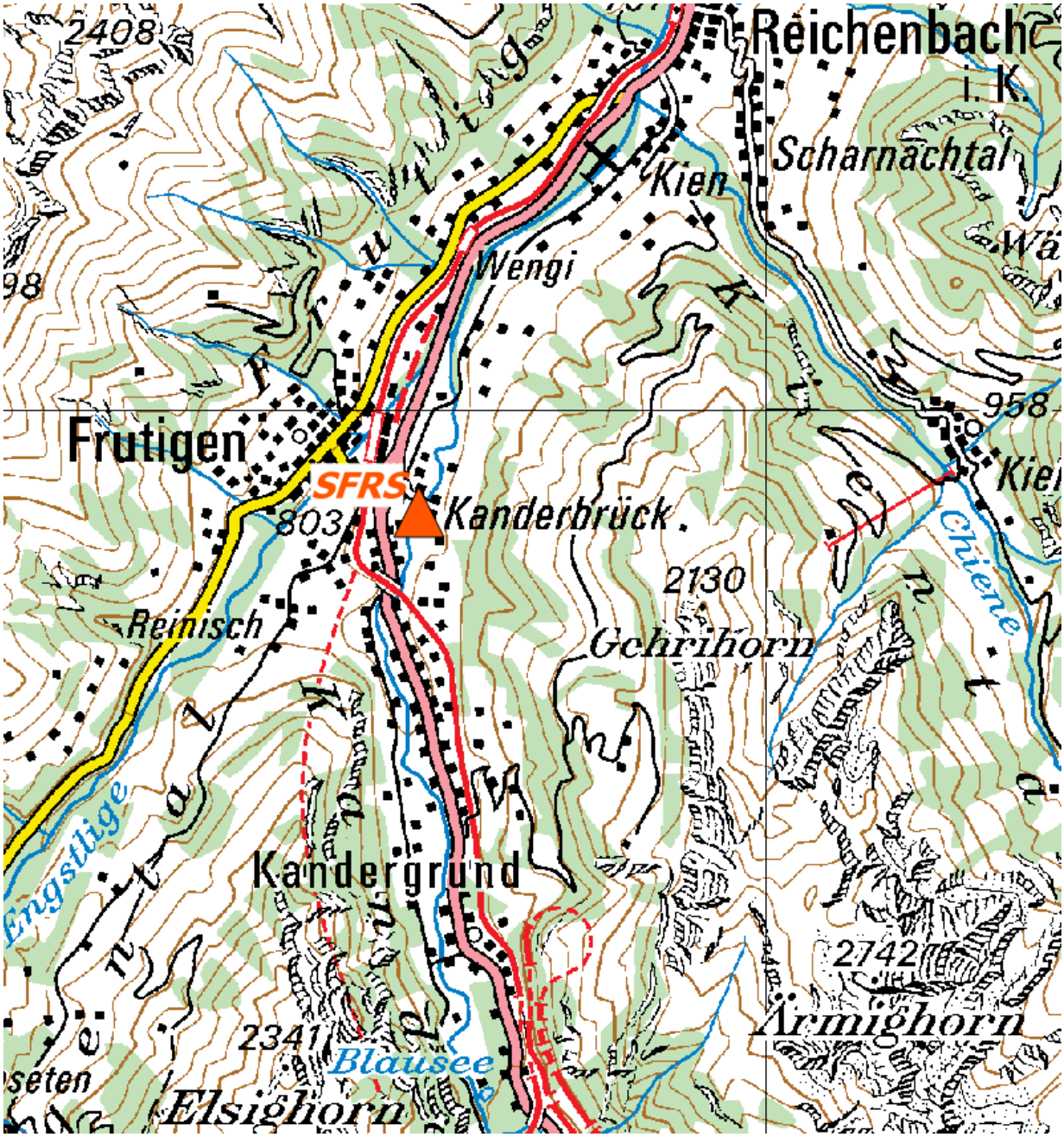

Figure 1: Map showing the location of station SFRS in Frutigen. The Lötschberg Base tunnel is the dashed red line departing from the railway track (red line) southwest of SFRS.

2 Geological setting

A geological map of the surroundings of station SFRS is shown in Fig. 2, with the sensor locations of the passive measurements. Station SFRS and all stations of the passive seismic array are located on alluvial deposits of the Kander river. Further east, river gravel deposits are found. The surrounding geology at the valley flanks is mainly composed of moraine.

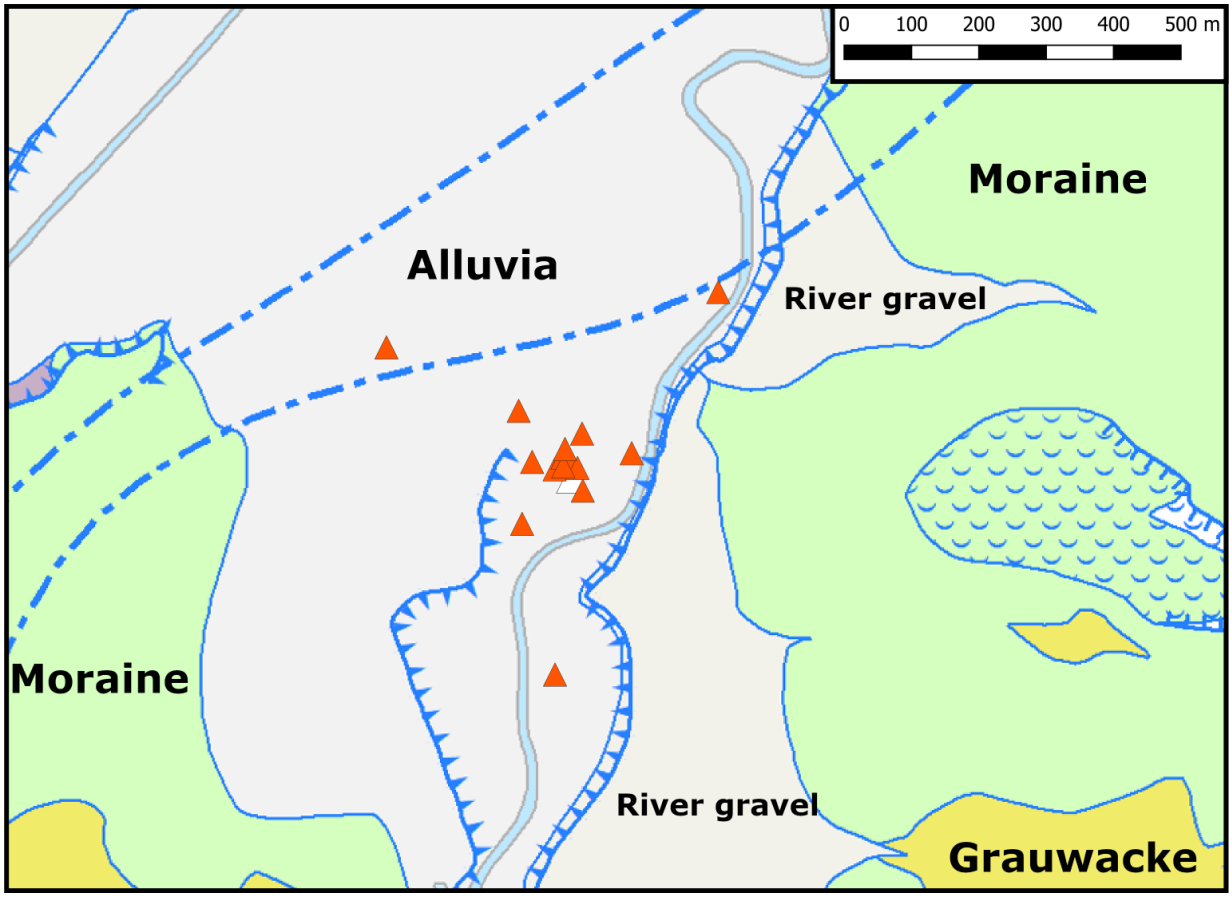

Figure 2: Geological map of the area around station SFRS, highlighting the location of the array stations (see next section). Source: Federal Office of Topography.

3 Site characterization measurements

3.1 Data set

In order to characterize the local underground structure around station SFRS, a passive seismic array measurement was carried out on 2 October 2020. The layout of the seismic measurement is shown in Fig. 3.
A single array measurement was performed. It was planned to consist of 16 stations, distributed in five rings of three stations each and a central station, with ring radii of 8 m, 20 m, 50 m, 105 m, and about 300 m, respectively.
The minimum and maximum inter-station distances of the final array deployment are 7.89 m and 619.8 m, respectively. The array recorded for 181 minutes.
The names of the stations of the array are composed of "SFRS" followed by a two-digit number (42 to 49, 52 to 55, 62, 73 to 75), indicating the serial number of the digitizers. Sensors with numbers above 60 were connected to the B channels of the respective digitizers and the numbers correspond to the serial number plus 20. All other sensors were connected to the respective A channels. The seismic stations consisted of Lennartz 3C 5 s sensors connected to Centaur digitizers.
The station locations were measured by a differential GPS system (Leica Viva GS10) which was set up to measure with a precision better than 5 cm. However, the GPS correction was not available during the measurement and the horizontal coordinates have uncertainties larger than 2 m. Therefore, the positions were corrected manually after the measurement, but the precision errors nevertheless reach up to 90 cm. The altitude values were then attributed to the horizontal positions using `map.geo.admin.ch`.

Figure 3: Layout of the array measurements around station SFRS (left) and zoom on the central part of the array (right). The location of SFRS is indicated by the white triangle, the locations of the stations for the passive seismic measurement by the orange triangles. Source: Federal Office of Topography.

3.2 H/V and RayDec ellipticity curves

Figure 4 shows the H/V curves determined with the time-frequency analysis method (Fäh et al., 2009) for all stations of the array. The curves are relatively similar and show a fundamental peak around 2.0 Hz. Station SFRS62, the station next to SFRS, has a peak frequency of 2.10 Hz. Stations SFRS48 with 2.49 Hz and SFRS52 with 2.81 Hz show higher fundamental frequencies. These stations are located to the northeast, close to the river and closer to the basin edge than the other stations. The smaller sediment thickness there is probably the reason for this higher fundamental frequency. At higher frequencies, a secondary peak is visible for most stations, but the frequencies are very different and represent the near-surface heterogeneities of the site.
The RayDec technique (Hobiger et al., 2009) is supposed to eliminate the contributions of other wave types than Rayleigh waves and give a better estimate of the ellipticity than the classical H/V technique. The RayDec ellipticity curves for all stations of the array measurements are shown in Fig. 4 and are similar to the H/V curves. For some curves, it seems that an ellipticity singularity is likely, for others this is not the case.

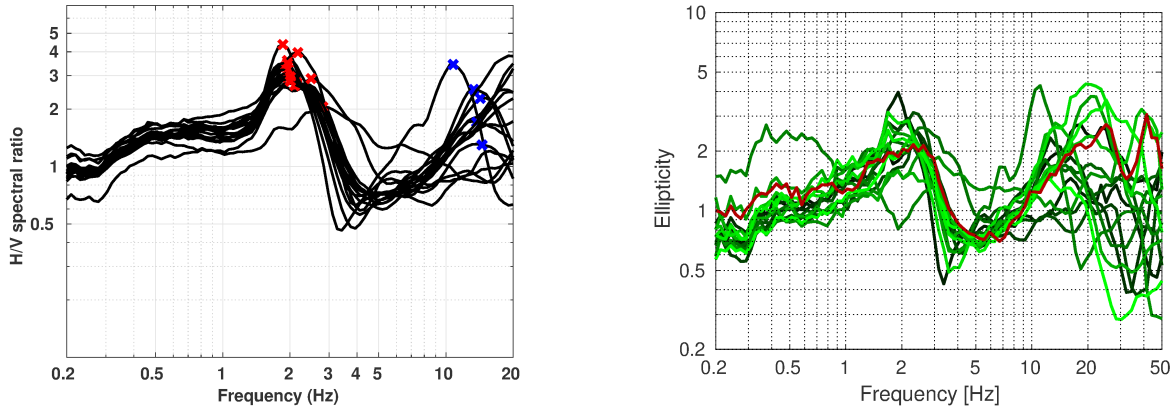

Figure 4: Left: Overview of the H/V measurements for the different stations of both array measurements. Right: RayDec ellipticities for all measurement stations. The red curve belongs to station SFRS62, the station next to the permanent station SFRS.

3.3 Polarization analysis

The polarization analysis was performed according to Burjánek et al. (2010) and Burjánek et al. (2012). The results for all stations are relatively similar. The results for SFRS62, the station closest to SFRS are shown here. No predominant azimuth and therefore no 2-dimensional polarization effects are visible.

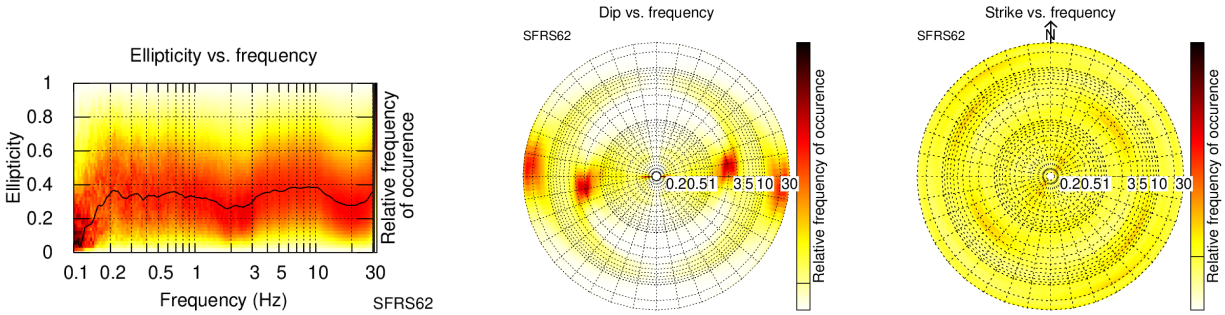

Figure 5: Polarization analysis of stations SFRS62.

3.4 SPAC

The SPAC (Aki, 1957) curves of the vertical components have been calculated using the M-SPAC (Bettig et al., 2001) technique implemented in geopsy. Rings with different radius ranges were defined and for all station pairs with distance inside this radius range, the cross-correlation was calculated over a wide frequency range. These cross-correlation curves are averaged for all station pairs of the respective ring and give the SPAC curves. The rings are defined in such a way that at least three station pairs contribute and that their connecting vectors have a good directional coverage.
The respective SPAC curves are shown in Fig. 6 and the dispersion curve obtained by inversion of the SPAC curves in Fig. 7. The dispersion curve is obtained between 2.7 and 14.4 Hz.

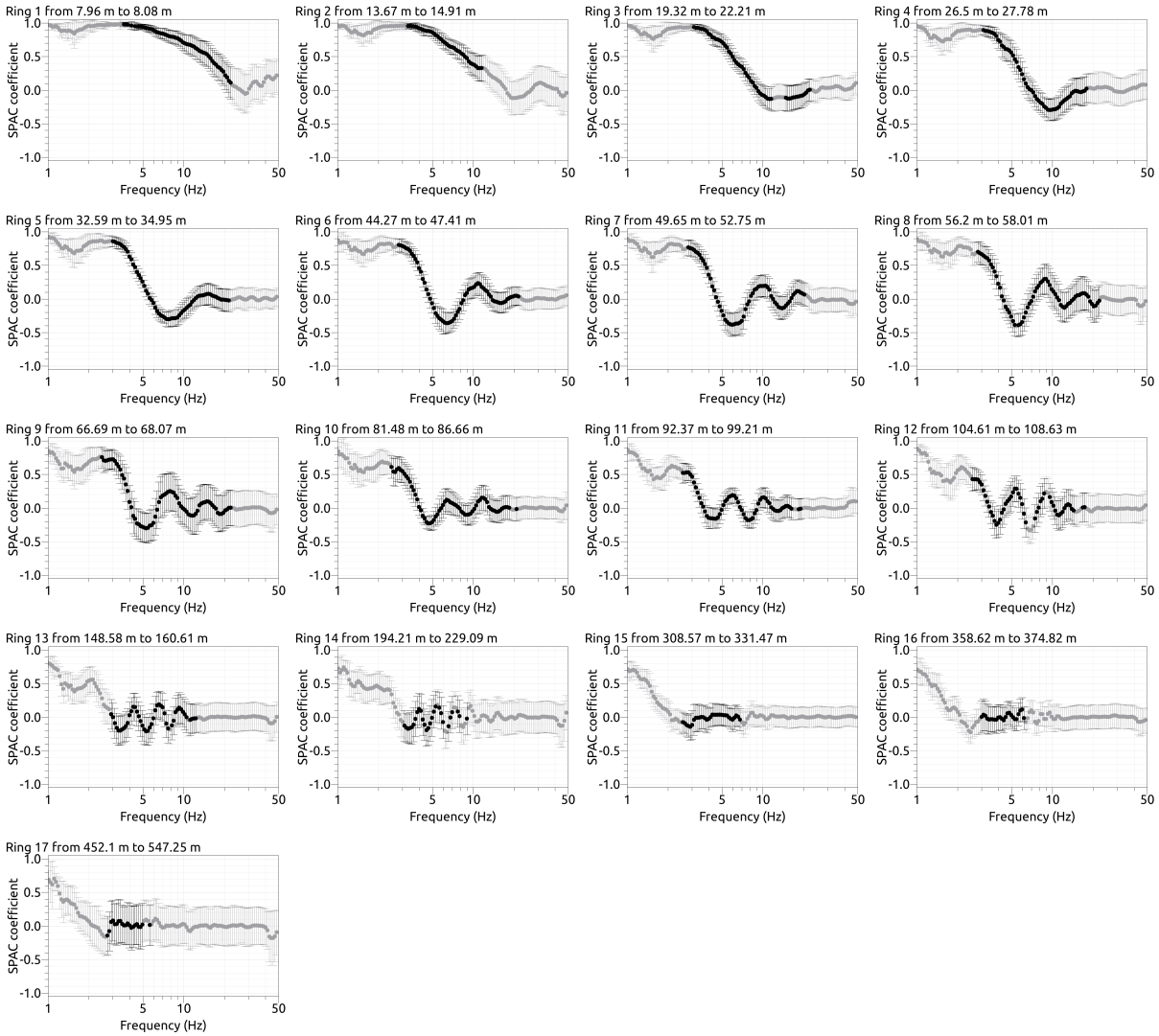

Figure 6: SPAC curves for the different station pairs. The black data points contributed to the dispersion curve estimation.

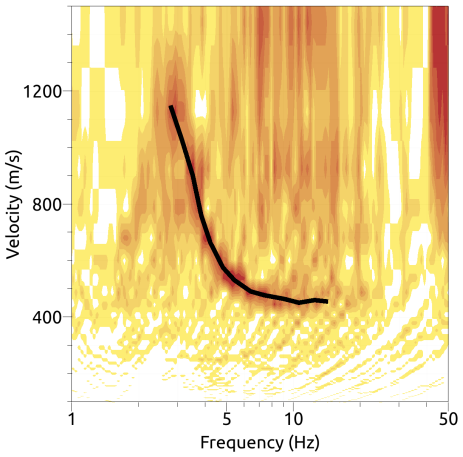

Figure 7: Resulting Rayleigh wave dispersion curve obtained by inversion of the SPAC curves of Fig. 6.

3.5 3-component high-resolution FK

The results of the 3-component high-resolution FK analysis (Poggi and Fäh, 2010) for the three arrays are shown in Fig. 8.
On the vertical component, corresponding to Rayleigh waves, we can clearly identify a continuous dispersion curve between 3.3 and 25.3 Hz. On the radial component, a first dispersion curve can be picked between 2.9 and 19.2 Hz. Another mode is visible mainly between 10.2 and 13.5 Hz, but its mode attribution seems difficult. On the transverse component, corresponding to Love waves, we can identify a continuous dispersion curve between 2.2 and 17.9 Hz.
The corresponding ellipticity curves for the vertical and radial dispersion curves are also clearly retrieved and will be compared with the single-station ellipticity curves at a later stage.

3.6 WaveDec

The results of the WaveDec (Maranò et al., 2012) processing are shown in Fig. 9. This technique estimates the properties of single or multiple waves simultaneously with a maximum likelihood approach. The parameter γ modifies the sharpness of the wave property estimation. In order to improve the results, a value of $\gamma = 0.2$ was used, corresponding to a predominantly maximum likelihood estimation.
A single Love wave dispersion curve is retrieved between 2.2 and 15.1 Hz.
For Rayleigh waves, a first dispersion curve is identified between 3.1 and 18.8 Hz. Small signs for another curve are visible between 11.4 and 13.5 Hz.
The ellipticity angle for the picked first Rayleigh wave dispersion curve is positive, i.e. corresponding to prograde particle motion, below about 3.6 Hz. Above, it is negative, i.e. retrograde, up to at least 10 to 15 Hz, where the polarization is unclear. For the second, very short dispersion curve, the particle motion is mostly horizontal and the ellipticity very high.

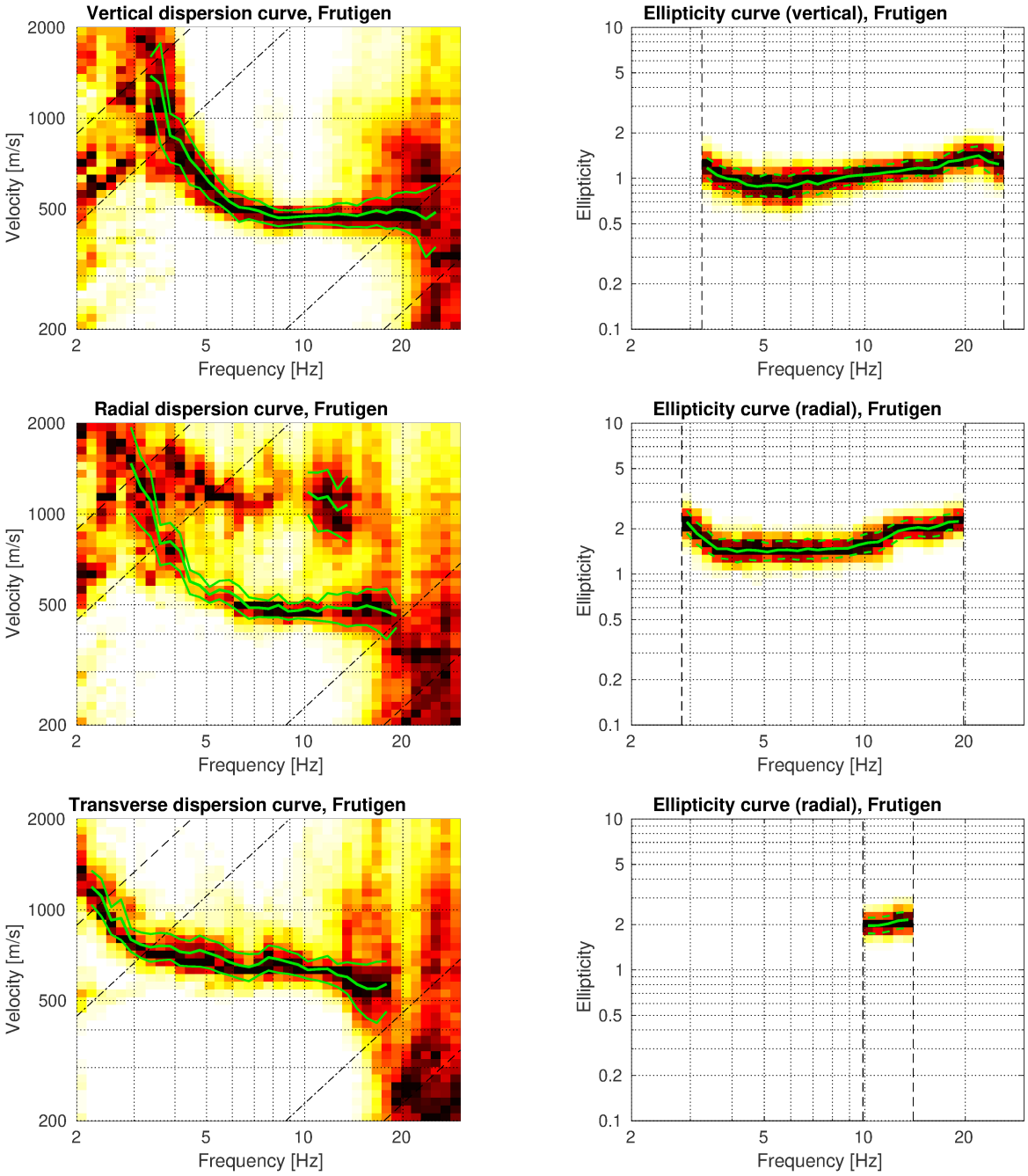

Figure 8: Dispersion curves obtained with the 3-component HRFK algorithm (Poggi and Fäh, 2010). On the left, from top to bottom, the dispersion curves for the transverse, vertical and radial components are shown, and on the right, the ellipticity curves for the vertical and radial components. The dashed and dotted black lines are the array resolution limits.

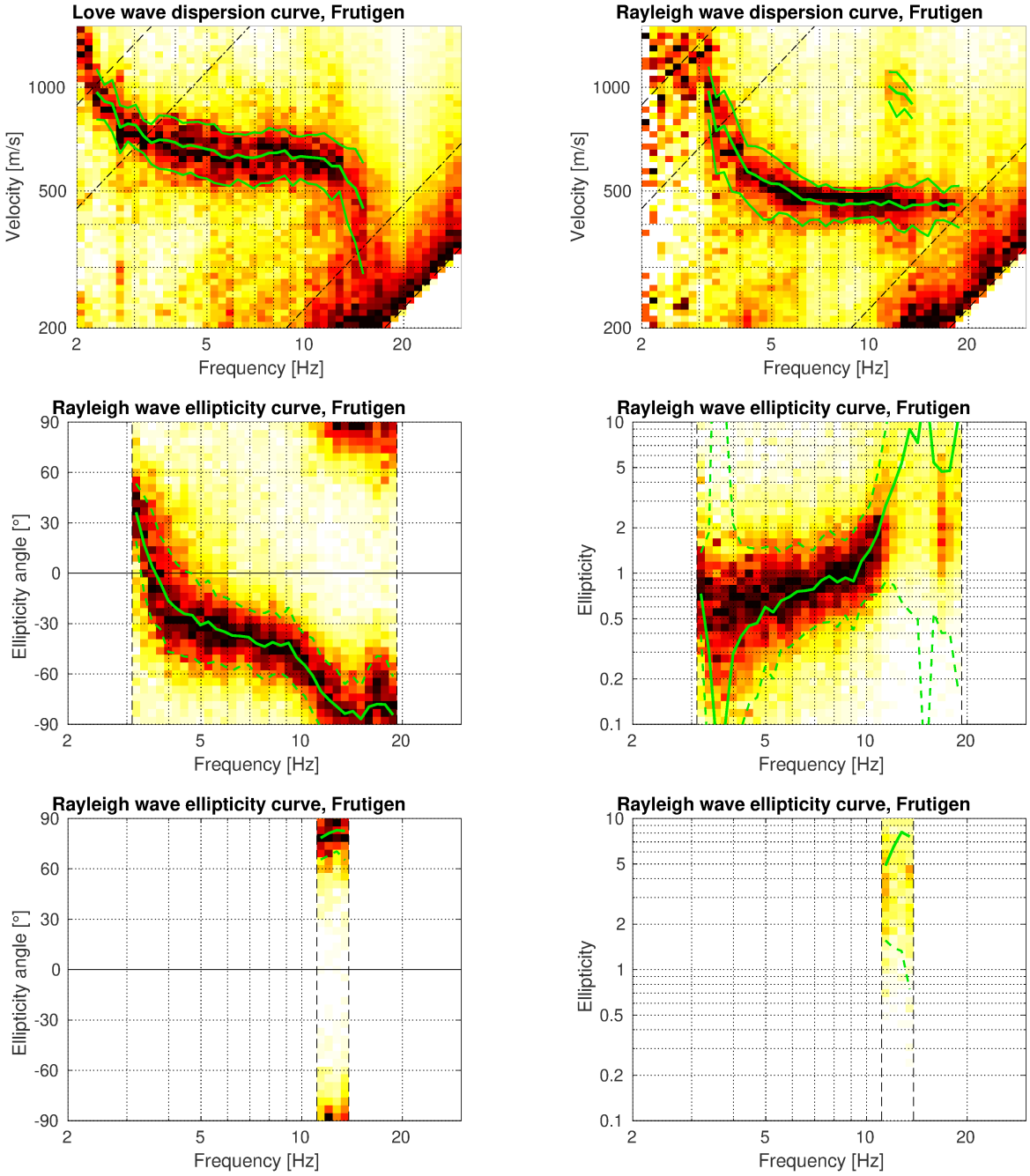

Figure 9: First line: Love (left) and Rayleigh (right) wave dispersion curves obtained with the WaveDec technique (Maranò et al., 2012). The dashed lines indicate the theoretical array resolution limits. Second and third line: Rayleigh wave ellipticity angle and ellipticity curves for the two identified dispersion curves.

3.7 Summary

Fig. 10 gives an overview of the dispersion and ellipticity curves determined by the different methods.
For Love waves, the HRFK and WaveDec curves are in good agreement, although WaveDec finds systematically lower velocities.
For Rayleigh waves, the different curves are also in good agreement, especially above 7 Hz. Below, the curves of the different methods have moderate differences.
The ellipticity curves have larger differences, but are still in good overall qualitative agreement. The vertical HRFK curve is in good agreement with the RayDec curve for station SFRS62. Between 5 and 10 Hz, the RayDec curve is in very good agreement with the WaveDec curve. The change in polarization sense around 3.6 Hz retrieved by WaveDec cannot be obtained by RayDec. At lower frequencies, the different curves are not in good agreement, at least partly because the array measurements for a heterogeneous underground differ from the single-station measurement for a given point.

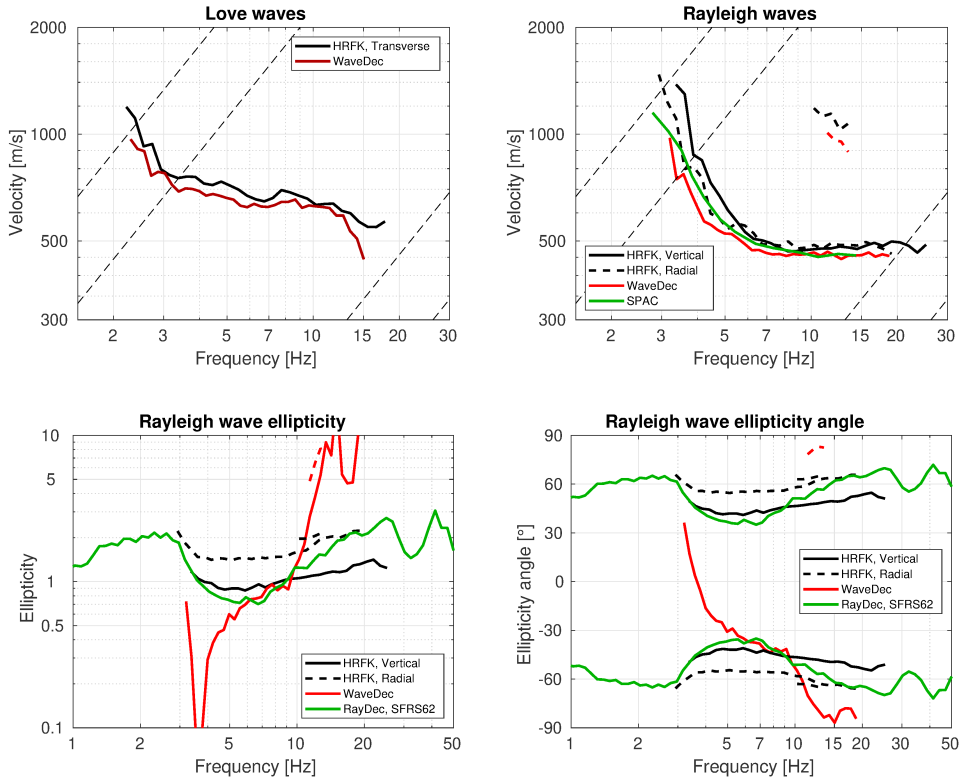

Figure 10: Overview of the Love and Rayleigh wave dispersion curves as well as the ellipticity and ellipticity angle curves for both arrays. The dashed lines indicate the theoretical resolution limits of array 3 (high frequencies) and array 1 (low frequencies). The RayDec ellipticity curves correspond to stations SFRS42 and SFRS46.

4 Data inversion

4.1 Inversion targets

The target curves for the inversion are shown in Fig. 11 and indicated in Table 1.
The retrieved Love wave dispersion curve is slower than the Rayleigh wave dispersion curve of the lowest mode for frequencies below about 4 Hz and faster above. Such a behavior is not possible to fit in the inversion process. We assume that the Rayleigh wave dispersion curve for the lower mode belongs to the fundamental mode. The curve retrieved on the radial component by 3C-HRFK lies in the middle of the vertical curve and the WaveDec curve and is in very good agreement with the SPAC curve and was therefore taken as target curve for the inversion.
The low-frequency 3C-HRFK curve for the transverse component below 3.4 Hz was assumed to be the fundamental mode, the high-frequency part above 7.8 Hz the first higher mode.
For the ellipticity angle, the WaveDec curve was used below 7 Hz and continued by the retrograde RayDec curve for SFRS62 between 7.3 and 25.3 Hz. The WaveDec curve is retrograde above 3.5 Hz and prograde below. Therefore, the ellipticity trough at this frequency is fixed in the inversion. The fundamental peak at the site is not forced in the inversion. It is not well visible in the RayDec curve for station SFRS62. The WaveDec curve is obtained by the array and therefore mostly representative for the center of the array, which is, however, very close to the permanent station.

Table 1: List of the different data curves used as target 1.

Method	Wave type	Mode	Curve type	Frequency range [Hz]
HRFK (T)	Love	fundamental	dispersion	2.29 - 3.35
HRFK (T)	Love	first higher	dispersion	7.87 - 17.34
HRFK (R)	Rayleigh	fundamental	dispersion	3.01 - 18.57
WaveDec	Rayleigh	fundamental	ellipticity angle	3.23 - 6.64
RayDec (SFRS62)	Rayleigh	fundamental	ellipticity angle (-)	7.35 - 25.28

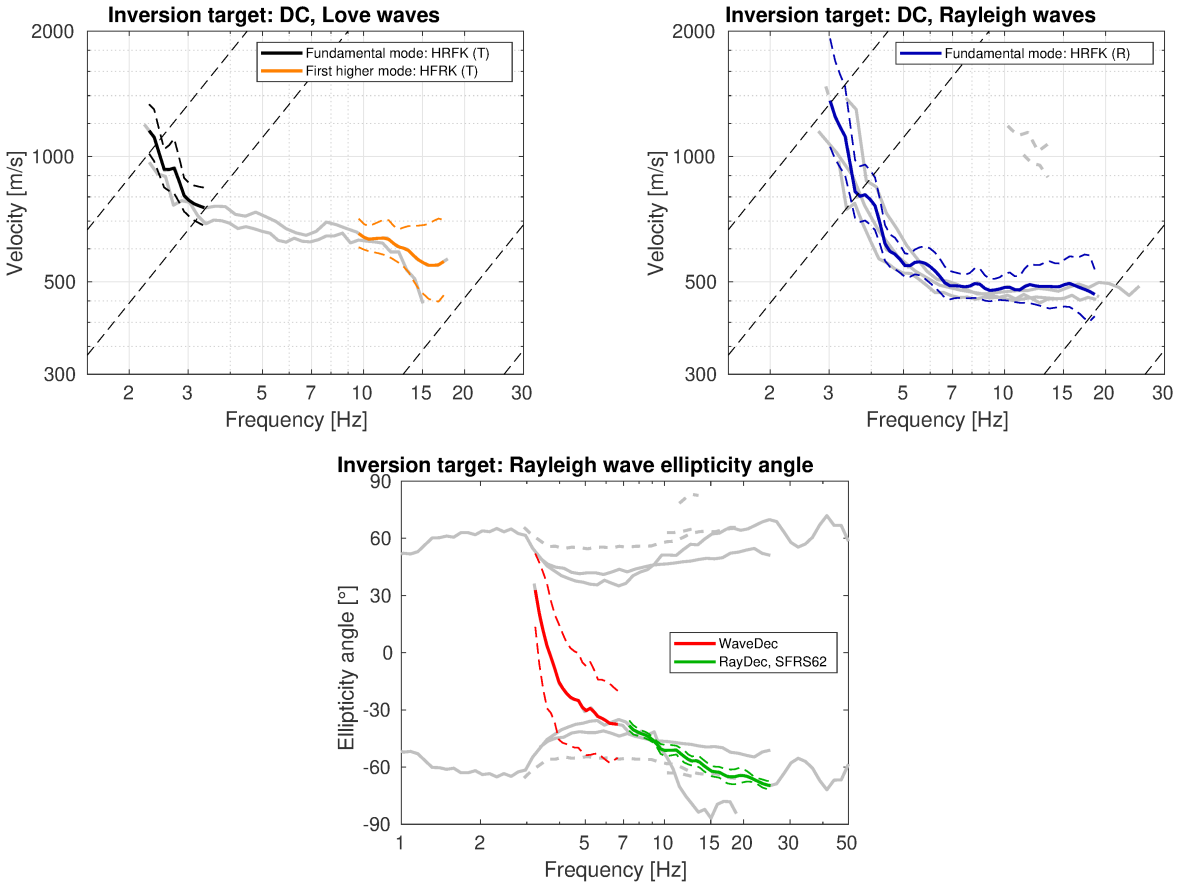

Figure 11: Overview of the dispersion and ellipticity angle curves used as targets 1 and 2 for the different inversions.

4.2 Inversion parameterization

For the inversions, seven different parameterizations were used in total. The first six have free values of the depths and velocities of the different layers, ranging from three to eight layers (including half-space). The last parameterization has fixed layer depths and consists of 20 layers in total. The P-wave velocities are allowed to vary up to 5000 m/s. The S-wave velocities are allowed to range from 30 to 3500 m/s. The deepest boundaries are allowed at a depth of 150 m maximum. The density is fixed to 2300 kg/m^3 for the lowest layer, to 1900 kg/m^3 for the superficial layer (or the first four layers in the fixed-layer case) and to 2100 kg/m^3 for all other layers. No low-velocity zones are allowed.

4.3 Inversion results

For each parameterization, 20 different runs were performed, but only the one giving the lowest minimum misfit was kept. In Table 2, the obtained minimum misfit values for these inversions are shown. In order to assure a good convergence of the solution, each inversion run for the 3-layer and 4-layer parameterization produced around 80 000 total models, for the 5-layer parameterization around 120 000 models, for the 6-layer parameterization around 160 000 models and for all other inversions around 200 000 models. The results of the inversions SFRS3l to SFRSfix are shown in Figs 12 - 18.
All inversions succeed in fitting the different curves in a good way, even if, for the inversions SFRS3l, SFRS4l and SFRSfix, the minimum misfit is slightly higher than for the other inversions. The fundamental peak of the Rayleigh wave ellipticity was not directly used in the inversions and constrained by the trough only, but the best models of all inversions show relatively similar ellipticity peak frequencies between 1.90 Hz and 2.01 Hz, which are in good agreement with the H/V and ellipticity curves shown in Fig. 4.

Table 2: List of inversions

Inversion	Number of layers	Number of models	Minimum misfit
SFRS3l	3	80 012	0.741
SFRS4l	4	80 006	0.737
SFRS5l	5	119 995	0.714
SFRS6l	6	160 003	0.710
SFRS7l	7	199 999	0.709
SFRS8l	8	200 018	0.709
SFRSfix	20	200 047	0.733

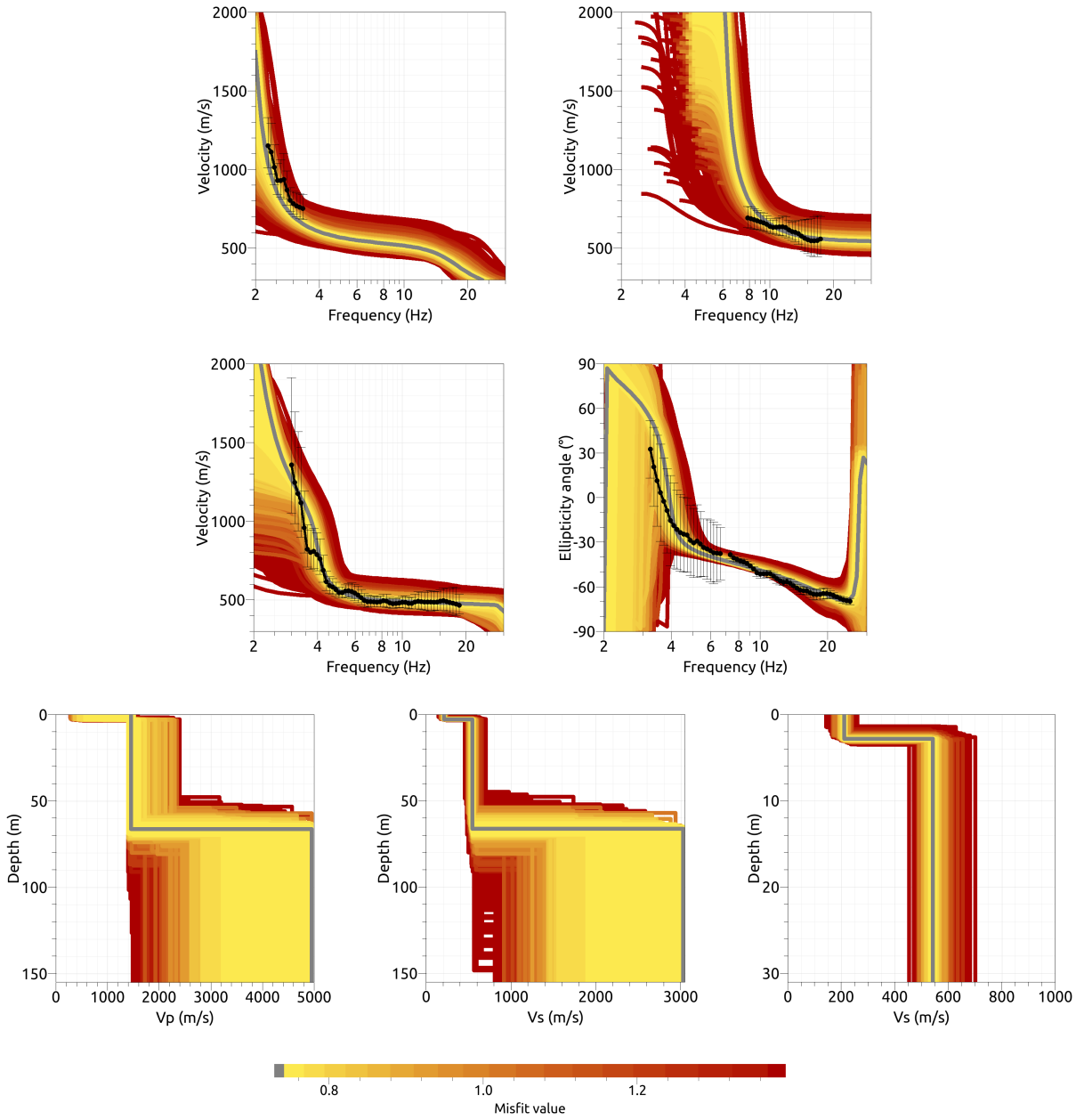

Figure 12: Inversion SFRS3l. Top line: Dispersion curves for the fundamental mode (left) and first higher mode (right) Love waves. Second line: Rayleigh wave dispersion curve (left) and ellipticity angle (right) for the fundamental mode. Bottom line: P-wave velocity profiles (left), S-wave velocity profiles (center and zoom on the upper 30 m on the right). All generated models are plotted on top of each other in the color corresponding to the respective misfit value. The black dots with error bars indicate the data points used for the inversion, the gray line indicates the best-fitting model.

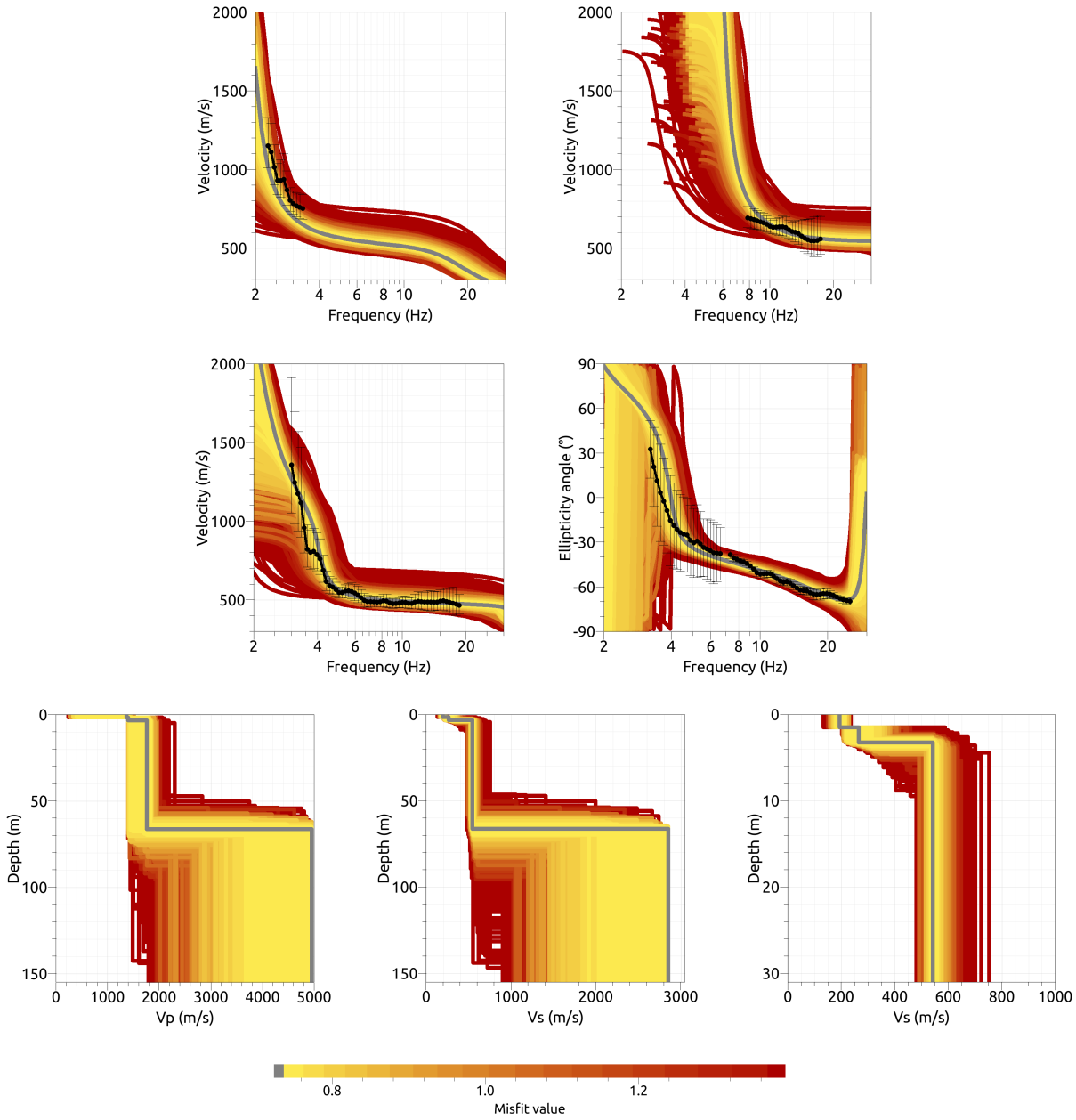

Figure 13: Inversion SFRS4l. Top line: Dispersion curves for the fundamental mode (left) and first higher mode (right) Love waves. Second line: Rayleigh wave dispersion curve (left) and ellipticity angle (right) for the fundamental mode. Bottom line: P-wave velocity profiles (left), S-wave velocity profiles (center and zoom on the upper 30 m on the right). All generated models are plotted on top of each other in the color corresponding to the respective misfit value. The black dots with error bars indicate the data points used for the inversion, the gray line indicates the best-fitting model.

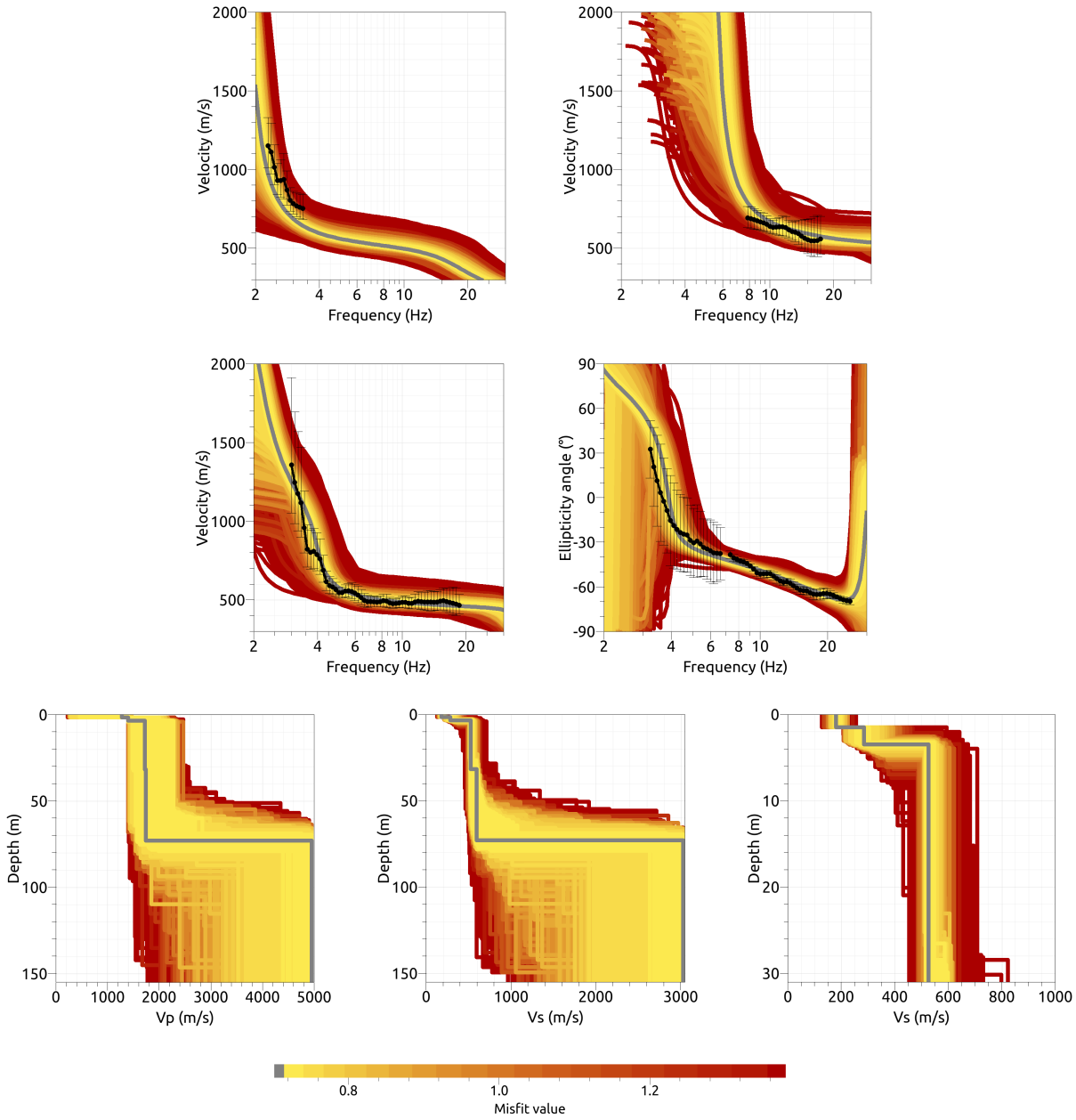

Figure 14: Inversion SFRS5l. Top line: Dispersion curves for the fundamental mode (left) and first higher mode (right) Love waves. Second line: Rayleigh wave dispersion curve (left) and ellipticity angle (right) for the fundamental mode. Bottom line: P-wave velocity profiles (left), S-wave velocity profiles (center and zoom on the upper 30 m on the right). All generated models are plotted on top of each other in the color corresponding to the respective misfit value. The black dots with error bars indicate the data points used for the inversion, the gray line indicates the best-fitting model.

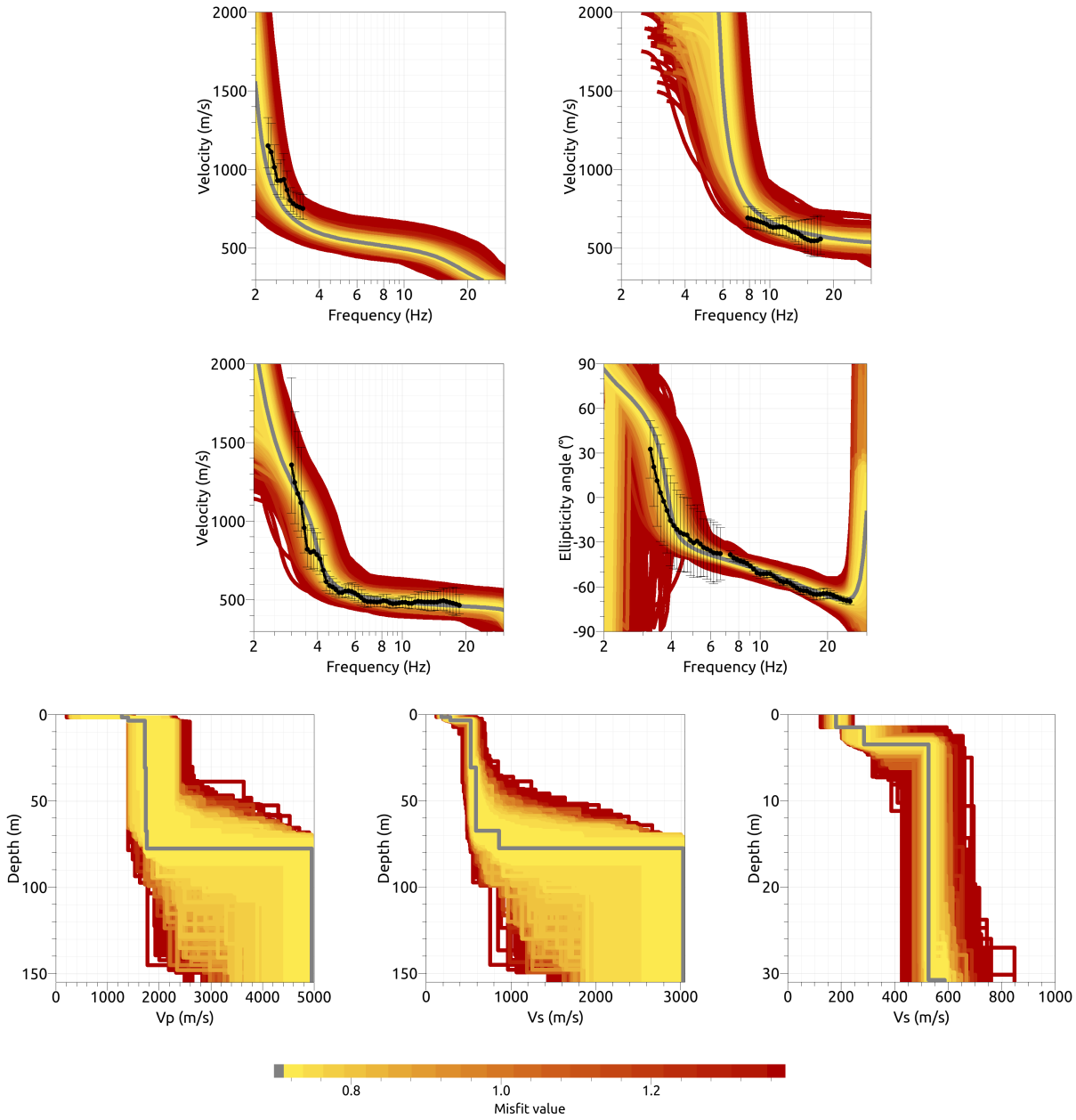

Figure 15: Inversion SFRS6l. Top line: Dispersion curves for the fundamental mode (left) and first higher mode (right) Love waves. Second line: Rayleigh wave dispersion curve (left) and ellipticity angle (right) for the fundamental mode. Bottom line: P-wave velocity profiles (left), S-wave velocity profiles (center and zoom on the upper 30 m on the right). All generated models are plotted on top of each other in the color corresponding to the respective misfit value. The black dots with error bars indicate the data points used for the inversion, the gray line indicates the best-fitting model.

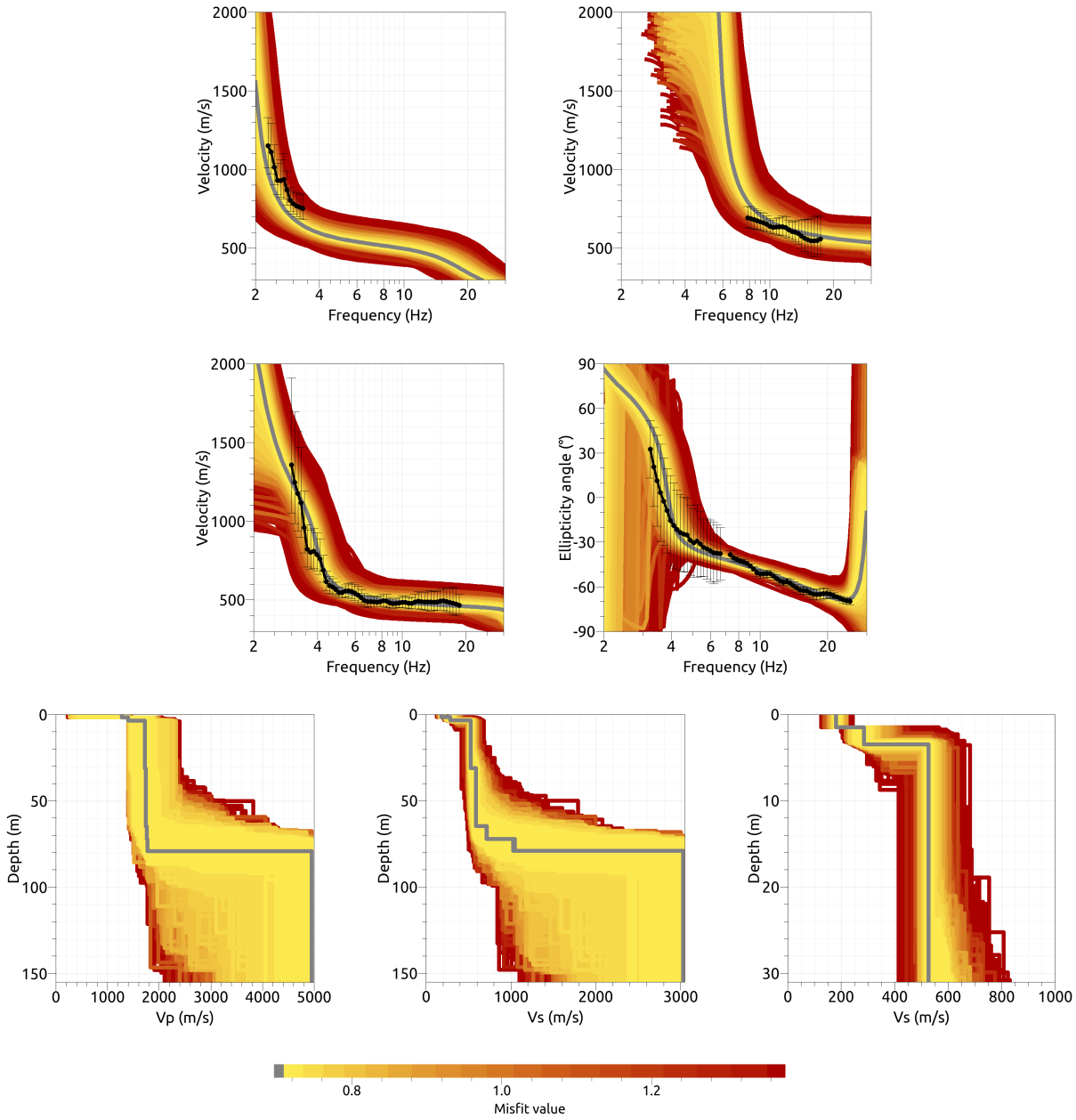

Figure 16: Inversion SFRS7l. Top line: Dispersion curves for the fundamental mode (left) and first higher mode (right) Love waves. Second line: Rayleigh wave dispersion curve (left) and ellipticity angle (right) for the fundamental mode. Bottom line: P-wave velocity profiles (left), S-wave velocity profiles (center and zoom on the upper 30 m on the right). All generated models are plotted on top of each other in the color corresponding to the respective misfit value. The black dots with error bars indicate the data points used for the inversion, the gray line indicates the best-fitting model.

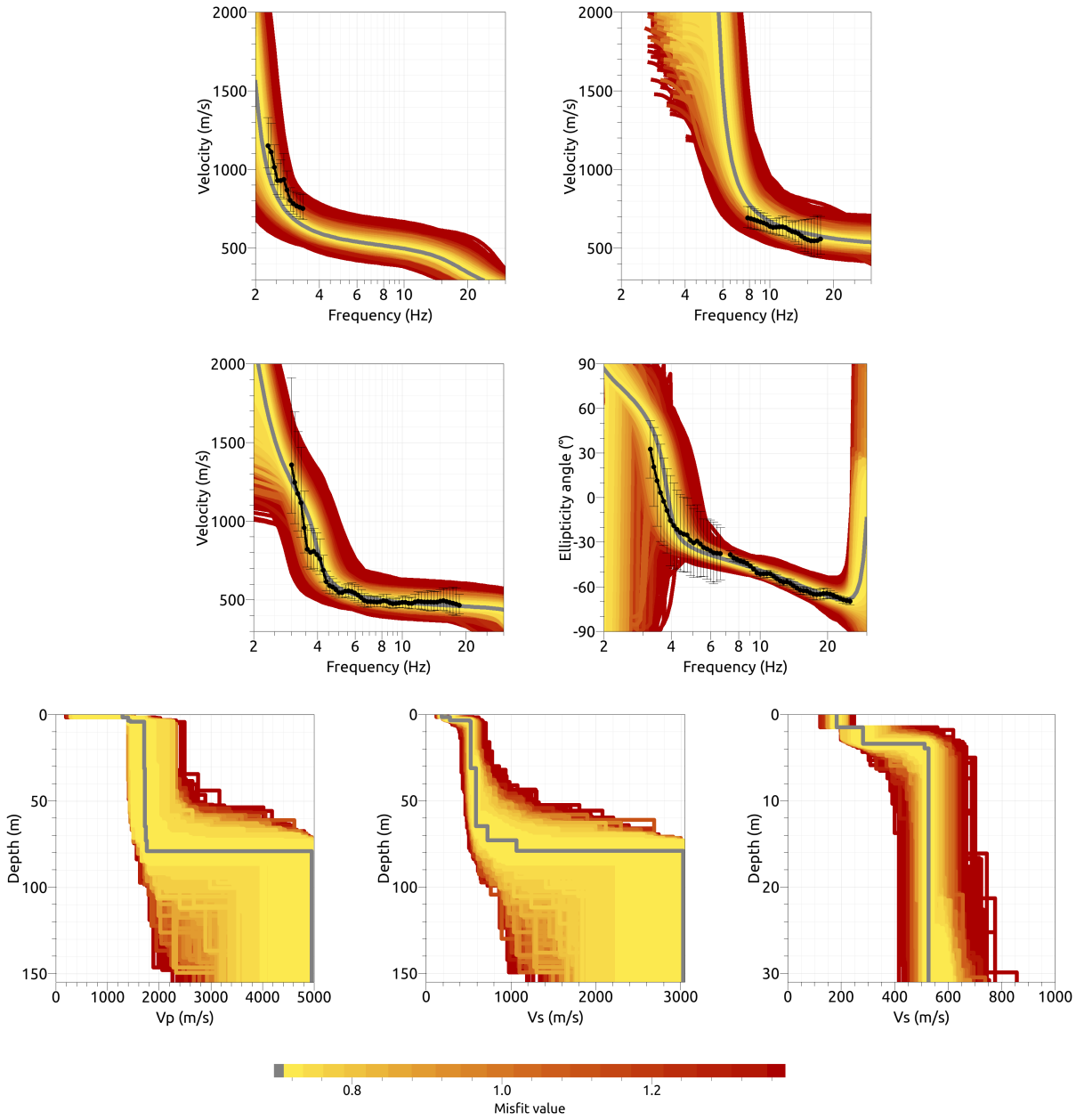

Figure 17: Inversion SFRS8l. Top line: Dispersion curves for the fundamental mode (left) and first higher mode (right) Love waves. Second line: Rayleigh wave dispersion curve (left) and ellipticity angle (right) for the fundamental mode. Bottom line: P-wave velocity profiles (left), S-wave velocity profiles (center and zoom on the upper 30 m on the right). All generated models are plotted on top of each other in the color corresponding to the respective misfit value. The black dots with error bars indicate the data points used for the inversion, the gray line indicates the best-fitting model.

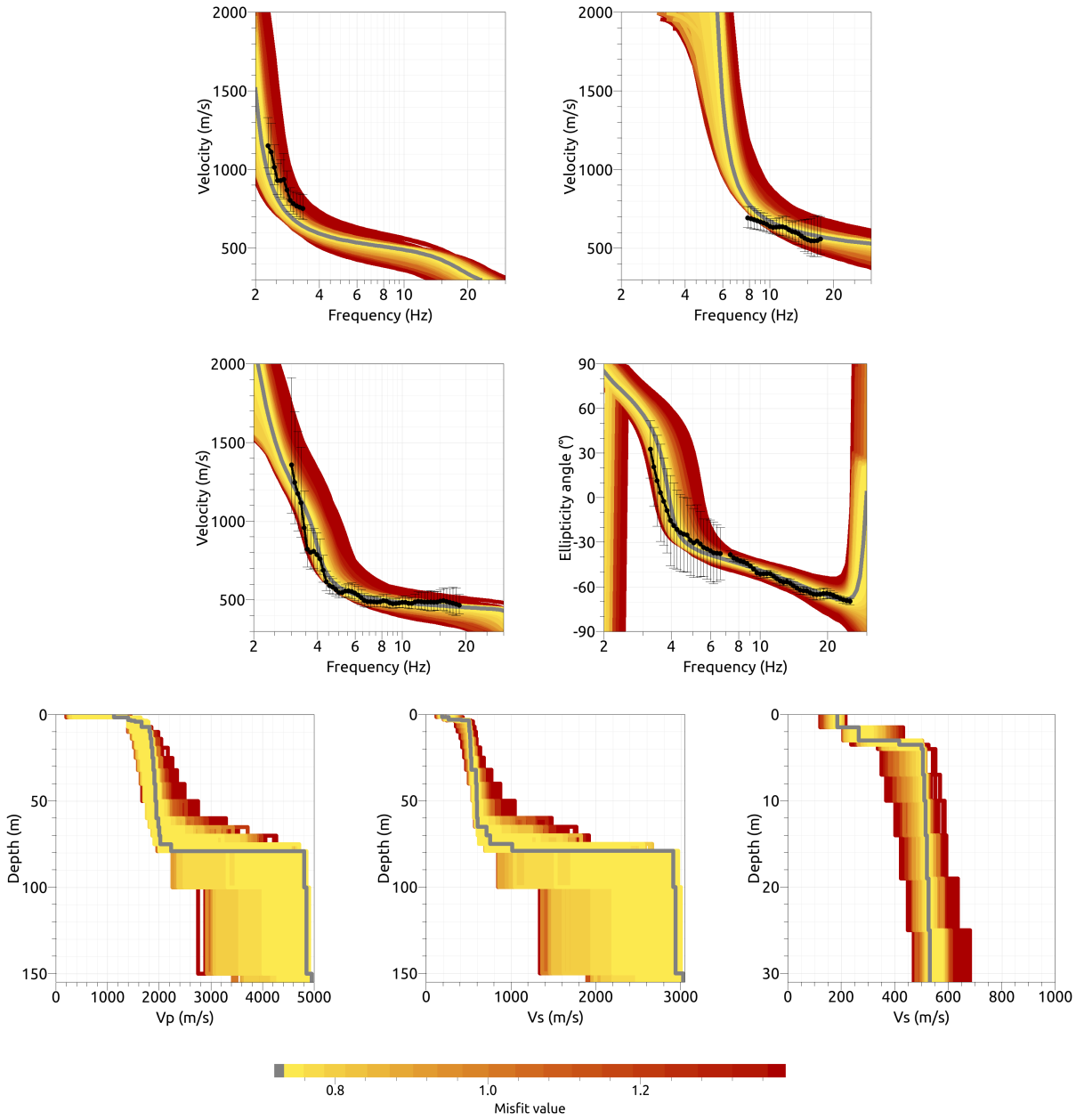

Figure 18: Inversion SFRSfix. Top line: Dispersion curves for the fundamental mode (left) and first higher mode (right) Love waves. Second line: Rayleigh wave dispersion curve (left) and ellipticity angle (right) for the fundamental mode. Bottom line: P-wave velocity profiles (left), S-wave velocity profiles (center and zoom on the upper 30 m on the right). All generated models are plotted on top of each other in the color corresponding to the respective misfit value. The black dots with error bars indicate the data points used for the inversion, the gray line indicates the best-fitting model.

4.4 Overview of the inversion result

The best-fitting models of all inversions are shown in Fig. 19. All parameterizations find two main velocity contrasts, a first shallow one at about 3 to 3.5 m depth and a second one at about 70 to 80 m depth. All inversions with at least four layers show that the first velocity contrast actually consists of two main contrasts, a first one at about 1.5 m, where the shear-wave velocity increases from around 180 m/s to around 280 m/s, and a second one at about 3 to 3.5 m, where the velocity increases to about 510 to 540 m/s. The highest frequency used in the inversion is about 25 Hz for the Rayleigh wave ellipticity and it corresponds to a wavelength of about 20 m. We cannot expect to resolve the near-surface structure in detail with such a wavelength. The lower velocity contrast, at a depth between 66 and 79 m, leads to velocities around 3000 m/s and can be identified as the seismic bedrock. In the different inversions, the bedrock velocity is not very well constrained, as the inclusion of the ellipticity information constrains the bedrock depths and the necessary contrast for a singularity in ellipticity. Nevertheless, all inversions seem to favor relatively high velocities. Nevertheless, this value seems too high for the bedrock at such depths.
The V_{S30} values for the best models of the different parameterizations range from 454 to 472 m/s, with an average value of (460.3 ± 7.2) m/s.
In EC8, this corresponds to soil class B. In SIA261, it can correspond to soil class B or C.

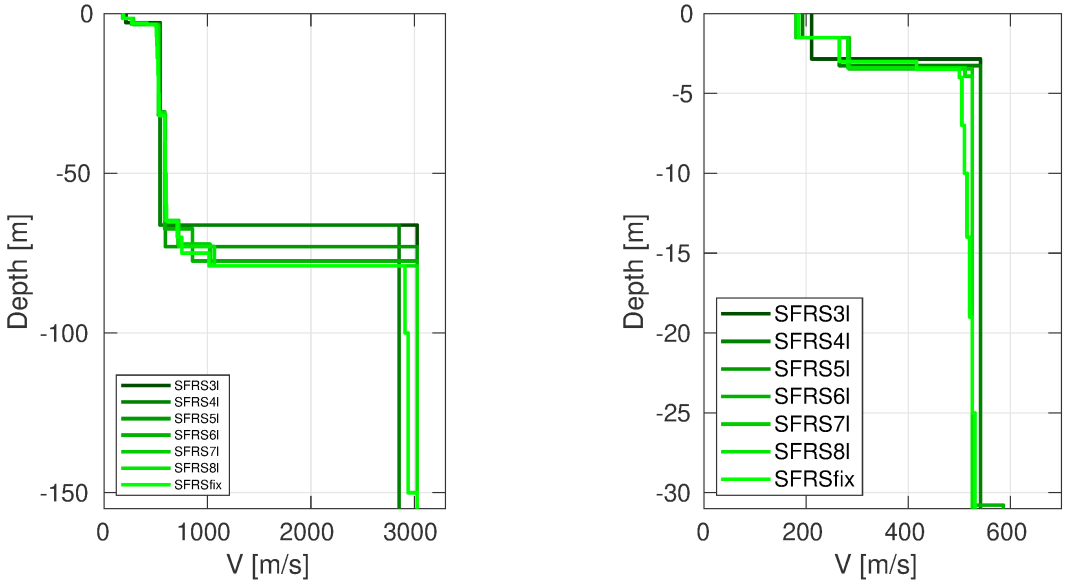

Figure 19: Overview of shear-wave velocity profiles of the best-fitting models of all inversions (left) and a zoom on the shallow part (right).

4.5 Site amplification

In Fig. 20, the theoretical amplification functions for the best models resulting from the different parameterizations for the two targets are compared with the empirical amplification for station SFRS, based on 57 events so far. The empirical amplification of the station increased to about 3 at 2 Hz and has values ranging mainly between 2 and 3 up to about 20 Hz. The modeled amplification fits the overall shape of the empirical one very well, although it contains some pronounced peaks at about 2 Hz, 6 Hz, 10 Hz, etc. These are caused by the 1D modeling, which is not realistic in an Alpine valley such as the one in Frutigen. For example, edge-generated surface waves are certainly present in the empirical amplification, but cannot be modeled in a 1D setting. Taking this into account, the similarity of empirical and modeled amplification can be considered as very good.

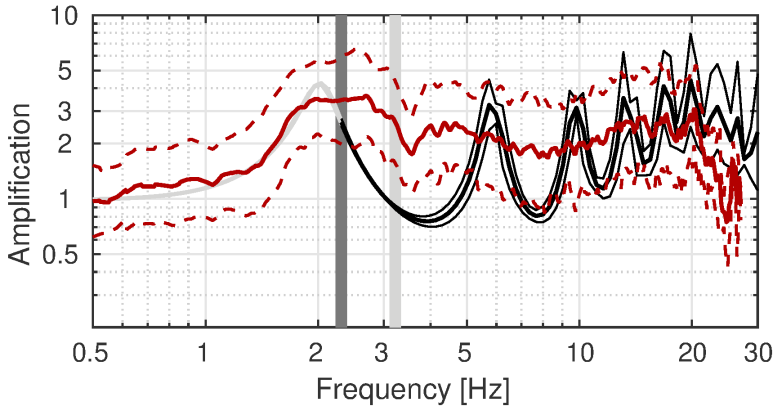

Figure 20: Comparison between the modeled amplification for the best models of the different inversions (black curve with standard deviation) and the empirical amplification measured at station SFRS (red, with standard deviation). The vertical light and dark grey bars correspond to the lowest frequency of the ellipticity and dispersion curves, respectively.

4.6 Quarter-wavelength representation

The quarter-wavelength velocity approach (Joyner et al., 1981) provides, for a given frequency, the average velocity at a depth corresponding to 1/4 of the wavelength of interest. It is useful to identify the frequency limits of the experimental data (the minimum frequency of the dispersion curve used in the inversions is 2.29 Hz, the minimum frequency with ellipticity information is about 3.23 Hz). The results using this proxy show that the dispersion curves constrain the profiles down to about 56 m, while the ellipticity information constrains it to about 38 m (Fig. 21). However, even if the fundamental peak at around 2.0 Hz is not included in the inversion targets, it is well constrained in the inversions because the trough is well constrained. Therefore, we can assume that the strong velocity contrast at a depth between 66 and 79 m is well constrained by the ellipticity data.
Moreover, the quarter wavelength impedance-contrast introduced by Poggi et al. (2012) is also displayed in the figure. It corresponds to the ratio between two quarter-wavelength average velocities, respectively from the top and the bottom part of the velocity profile, at a given frequency (Poggi et al., 2012). This curve shows a strong contrast at the fundamental frequency of the site.

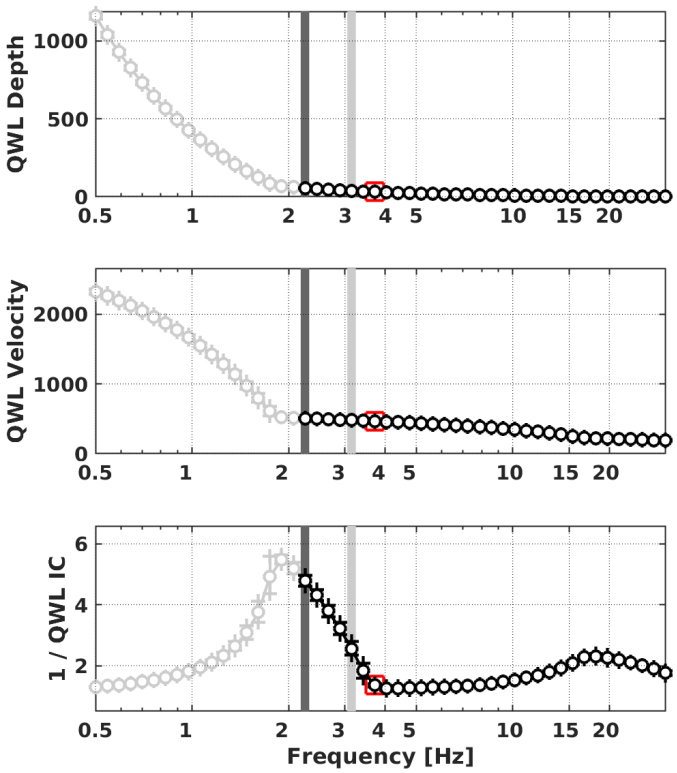

Figure 21: Quarter wavelength representation of the velocity profile for the best models of the inversions (top: depth, center: velocity, bottom: inverse of the impedance contrast). The black curves are constrained by the dispersion curves, the light grey curves are not constrained by the data. The red square corresponds to V_{S30}.

5 Conclusion

We performed a passive array measurement to characterize the soil underneath station SFRS in Frutigen (BE), located in the sedimentary basin of the Kander river.
The H/V and Rayleigh wave ellipticity measurements indicate that the fundamental frequency of the site is about 2.0 Hz. Using the array measurements, we could retrieve dispersion curves for Love and Rayleigh waves. The Rayleigh wave dispersion curve was interpreted as the fundamental mode, while the Love wave dispersion curves were interpreted as partly the fundamental and partly the first higher mode.
Inversions using the dispersion curves and the ellipticity angle as targets were performed. The underground can be mainly characterized by a single or two near-surface layers in the superficial about 3.5 m, followed by another layer with shear-wave velocity of about 510 to 540 m/s down to a depth of about 66 to 79 m, where the seismic bedrock with a velocity of about 3000 m/s is found, even if this value is probably not well constrained by the inversions.
The V_{S30} value is (460.3 ± 7.2) m/s. In EC8, this corresponds to soil class B. In SIA261, it corresponds to soil class C.

Acknowledgements

The authors thank Nora Schweizer for her help during the array measurements.

References

Aki, K. (1957). Space and time spectra of stationary stochastic waves, with special reference to microtremors. *Bull. Earthquake Res. Inst. Tokyo Univ.*, 35:415–456.

Bettig, B., Bard, P.-Y., Scherbaum, F., Riepl, J., Cotton, F., Cornou, C., and Hatzfeld, D. (2001). Analysis of dense array noise measurements using the modified spatial auto-correlation method (SPAC): application to the Grenoble area. *Boll. Geof. Teor. Appl.*, 42:281–304.

Burjánek, J., Gassner-Stamm, G., Poggi, V., Moore, J. R., and Fäh, D. (2010). Ambient vibration analysis of an unstable mountain slope. *Geophys. J. Int.*, 180:820–828.

Burjánek, J., Moore, J. R., Molina, F. X. Y., and Fäh, D. (2012). Instrumental evidence of normal mode rock slope vibration. *Geophys. J. Int.*, 188:559–569.

Fäh, D., Wathelet, M., Kristekova, M., Havenith, H., Endrun, B., Stamm, G., Poggi, V., Burjanek, J., and Cornou, C. (2009). Using ellipticity information for site characterisation. NERIES deliverable JRA4 D4, available at http://www.neries-eu.org.

Hobiger, M., Bard, P.-Y., Cornou, C., and Le Bihan, N. (2009). Single station determination of Rayleigh wave ellipticity by using the random decrement technique (RayDec). *Geophys. Res. Lett.*, 36.

Joyner, W. B., Warrick, R. E., and Fumal, T. E. (1981). The effect of Quaternary alluvium on strong ground motion in the Coyote Lake, California, earthquake of 1979. *Bull. Seismol. Soc. Am.*, 71(4):1333–1349.

Maranò, S., Reller, C., Loeliger, H.-A., and Fäh, D. (2012). Seismic waves estimation and wavefield decomposition: Application to ambient vibrations. *Geophys. J. Int.*, 191:175–188.

Poggi, V., Edwards, B., and Fäh, D. (2012). Characterizing the Vertical-to-Horizontal ratio of ground motion at soft-sediment sites. *Bull. Seismol. Soc. Am.*, 102(6):2741–2756.

Poggi, V. and Fäh, D. (2010). Estimating Rayleigh wave particle motion from three-component array analysis of ambient vibrations. *Geophys. J. Int.*, 180:251–267.